



# The composite sphere of manganese oxide and carbon nanotubes as a prospective anode material for lithium-ion batteries



Xiaofei Sun<sup>a</sup>, Youlong Xu<sup>a,\*</sup>, Peng Ding<sup>a,b</sup>, Guogang Chen<sup>a</sup>, Xiaoyu Zheng<sup>a</sup>, Rui Zhang<sup>a</sup>, Long Li<sup>a</sup>

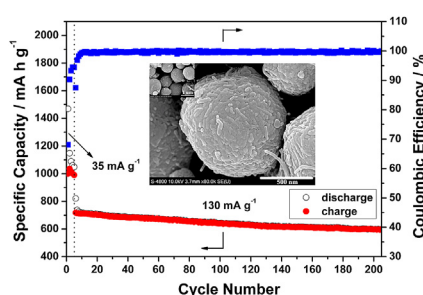
<sup>a</sup>Electronic Materials Research Laboratory, Key Laboratory of the Ministry of Education & International Center for Dielectric Research, Xi'an Jiaotong University, Xi'an 710049, China

<sup>b</sup>Department of Power, Wuhan Ordnance Non-Commissioned Officer Academy, Wuhan 430075, China

## HIGHLIGHTS

- Microsphere MnO is prepared by simple decomposition of MnCO<sub>3</sub>.
- MnO shows better electrochemical performance than MnCO<sub>3</sub>.
- Both the performances of MnCO<sub>3</sub> and MnO could be improved by supporting with CNTs.
- The MWNTs/MnO composite shows superior capacitive, rate and cycling performances.

## GRAPHICAL ABSTRACT



## ARTICLE INFO

### Article history:

Received 20 November 2013

Received in revised form

14 December 2013

Accepted 27 December 2013

Available online 4 January 2014

### Keywords:

Manganese oxide  
Manganese carbonate  
Carbon nanotubes  
Conversion reaction  
Anode  
Lithium ion battery

## ABSTRACT

Transition metal oxides and carbonates are emerging anode materials for lithium-ion batteries based on conversion reactions. In this paper, MnO sphere is simply prepared by decomposition of the spherical MnCO<sub>3</sub> precursor, and multi-walled carbon nanotubes (MWNTs) are employed to modify their lithium storage capabilities. It is found that the MnO system has superior battery performance over MnCO<sub>3</sub> although both of their performances could be significantly improved by carbon nanotube backbones. In particular, the MWNTs/MnO composite sphere shows an outstanding electrochemical performance with a comparatively lower lithium extraction potential. The reversible specific capacity at 35 mA g<sup>-1</sup> is ~1005 mA h g<sup>-1</sup> with an initial coulombic efficiency of ~68%. After 200 cycles at 130 mA g<sup>-1</sup>, the capacity is slowly decreased from ~722 mA h g<sup>-1</sup> to ~597 mA h g<sup>-1</sup> indicating a retention of ~83%. Under a high current rate of 715 mA g<sup>-1</sup> (~1.6 C), it could still deliver ~447 mA h g<sup>-1</sup>. The high conductivity of MWNTs, unique spherical morphology of the composite, facile electron and Li<sup>+</sup> transportations in the electrode/electrolyte interface, self-accommodation of the large volume change during discharge/charge and synergetic lithium storage from each component are ascribed for the advanced performance.

© 2014 Elsevier B.V. All rights reserved.

## 1. Introduction

Due to the high specific capacity, long cycling life and fast charge/discharge rate, lithium-ion battery has been widely used in portable electronic devices, and is being intensively explored in high efficiency energy storage applications such as electric vehicles (EVs) to meet the increasing global energy and environmental crisis

\* Corresponding author. No. 28, West Xianning Road, Xi'an 710049, China. Tel./fax: +86 29 82665161.

E-mail address: [ylxu@mail.xjtu.edu.cn](mailto:ylxu@mail.xjtu.edu.cn) (Y. Xu).

[1,2]. The current anode material for commercial lithium-ion battery is mostly still graphite-based carbon as was invented. However, the low volumetric capacity and potential safety issue constrain the broad application of carbon anode in next generation high energy/power lithium-ion batteries [3]. A large number of novel materials such as  $\text{Li}_4\text{Ti}_5\text{O}_{12}$  [4], Sn [5], Si [6] and transition metal oxides  $\text{MO}_x$  ( $M = \text{Fe}, \text{Co}, \text{Ni}, \text{Cu}, \text{Mn}, \text{etc.}$ ) [7] have emerged in recent years as alternative anode candidates. Poizot [8] et al. first reported the attractive lithium storage capability of  $\text{MO}_x$  via conversion reactions [9] during  $\text{Li}^+$  insertion/extraction. When used in lithium-ion batteries, such metal oxides exhibit high theoretical capacities but sluggish reaction kinetics during discharge/charge, therefore, a large potential hysteresis ( $\sim 1.0$  V) is usually generated. In addition, the low electric conductivity and large volume change during  $\text{Li}^+$  incorporation/extraction make them far away from large scale commercialization.

Among various transition metal oxides  $\text{MO}_x$ , manganese monoxide MnO has a relatively small potential hysteresis ( $\sim 0.7$  V) [10], high specific capacity (theoretically  $755.6 \text{ mA h g}^{-1}$ ), low electromotive force (1.032 V vs.  $\text{Li}/\text{Li}^+$  hereafter) [11] and high density ( $5.43 \text{ g cm}^{-3}$ ) [12], therefore, is a perspective anode material for lithium-ion batteries [13]. However, like other  $\text{MO}_x$ , the capacitive, rate and cycling performances are severely deteriorated by the low electric conductivity and large volume change during  $\text{Li}^+$  incorporation/extraction [14]. Particle down-sizing and carbon coating are introduced as common routes to improve the electrochemical performance of MnO [10]. For example, Ding [15] et al. prepared pure nano-MnO by a simple solid state reaction method which shows a reversible capacity of  $679.7 \text{ mA h g}^{-1}$ ,  $584.5 \text{ mA h g}^{-1}$  and  $290 \text{ mA h g}^{-1}$  between 0.01 V and 3.0 V at the current density of  $46.3 \text{ mA g}^{-1}$ ,  $141.1 \text{ mA g}^{-1}$  and  $494.7 \text{ mA g}^{-1}$ , respectively. Liu [16] et al. further coated a carbon layer on the surface of nano-sized MnO, and increased the reversible capacity to  $\sim 700 \text{ mA h g}^{-1}$ ,  $320 \text{ mA h g}^{-1}$  and  $235 \text{ mA h g}^{-1}$  between 0.01 V and 2.0 V (note the narrower potential window) at the current density of  $75 \text{ mA g}^{-1}$ ,  $375 \text{ mA g}^{-1}$  and  $755 \text{ mA g}^{-1}$ , respectively. Moreover, nano-structure design [17,18], e.g., nanoplate [19], nanotube [20,21], nanoflake [22], nanosheet [23,24], nanofiber [25], hollow sphere [26] and nanocrystalline thin film [27,28], shows great potential in modification of the physicochemical properties thus the battery performance of MnO.

In the previous work, we demonstrated the remarkable performance advancement of MnO rods by introducing carbon nanotubes (CNTs) [29], and the electrochemical performance was further improved by forming a CNTs/MnO/C hybrid matrix [30]. Comparing with graphene anchored MnO that exhibits similar performance, CNTs are much more cost-effective. In this paper, the composite spheres of multi-walled carbon nanotubes and manganese monoxide (MWNTs/MnO) are prepared by thermal decomposition of the MWNTs/ $\text{MnCO}_3$  precursor. The battery performances of MnO spheres with/without MWNTs are comparatively studied, and that of the  $\text{MnCO}_3$  and MWNTs/ $\text{MnCO}_3$  precursors are discussed as well.

## 2. Experimental

The multi-walled carbon nanotubes were purchased from Shenzhen Nanotech Port Co., Ltd, and were pretreated in a mixed solution of  $\text{H}_2\text{SO}_4/\text{HNO}_3$  (3/1, volume ratio) before usage [31,32]. 0.12 g so-functionalized MWNTs were dispersed in 100 mL deionized water by ultrasonication for 2 h. A little ethanol and OP-10 (polyoxyethylene octylphenol ether) surfactant were added to enhance the solubility of MWNTs. 0.845 g reagent grade  $\text{MnSO}_4 \cdot \text{H}_2\text{O}$  was added at  $4^\circ\text{C}$  followed by vigorous stirring for 12 h. 100 mL  $0.4 \text{ mol L}^{-1}$   $\text{NH}_4\text{HCO}_3$  aqueous solution, which was

also prepared at  $4^\circ\text{C}$  by magnetic stirring, was added with continuous stirring at  $4^\circ\text{C}$  for 2 h. The precipitated MWNTs/ $\text{MnCO}_3$  was collected by repeated filtration and washing, and was dried at  $80^\circ\text{C}$  for 12 h under vacuum. The MWNTs/ $\text{MnCO}_3$  composite was sintered at  $700^\circ\text{C}$  for 3 h under argon (Ar) protection to synthesize MWNTs/MnO. Pure  $\text{MnCO}_3$  was prepared by simply precipitating  $\text{MnSO}_4 \cdot \text{H}_2\text{O}$  and  $\text{NH}_4\text{HCO}_3$  without adding MWNTs, and the corresponding bare MnO was obtained by the same calcination process as described above.

Powder X-ray diffraction (XRD) was performed on an X'Pert Pro (PANalytical) with  $\text{Cu K}\alpha$  radiation. Field emission scanning electron microscopy (FESEM, Hitachi S-4800) was used to observe the particle size and morphology. A thin platinum (Pt) layer was deposited for better freezing of the FESEM images. The chemical elements were detected by the energy dispersive X-ray spectroscopy (EDX) attached to the FESEM. The tap density was measured by a JZ-7 Powder Tap Density Analyzer (Chengdu Jingxin Instruments Co. Ltd.).

CR2016 coin cells were fabricated to study the electrochemical performances. Lithium metal was used as the counter electrode, and the electrolyte was  $1 \text{ mol L}^{-1}$   $\text{LiPF}_6$  in ethylene carbonate/dimethyl carbonate (EC/DMC, 1/1). The working electrode was consisted of 70 wt.% active material ( $\text{MnCO}_3$ , MnO, MWNTs/ $\text{MnCO}_3$ , MWNTs/MnO), 20 wt.% acetylene black and 10 wt.% polyvinylidene fluoride (PVDF). The prototype batteries were made in an Ar-filled glove box under rigid water and oxygen monitoring, and were galvanostatically discharged/charged at room temperature between 0.01 V and 3 V on a CT2001A Land Battery Testing System. The specific capacities of MWNTs/ $\text{MnCO}_3$  and MWNTs/MnO are calculated by the total weights of the composites throughout this paper, i.e. the weights of MWNTs are not excluded. The electrochemical impedance spectroscopy (EIS) was carried out by a Versatile Multichannel Galvanostat 2/Z (VMP2, Princeton Applied Research) in the frequency range from  $10^5 \text{ Hz}$  to  $10^{-2} \text{ Hz}$ .

## 3. Results and discussion

As shown by powder X-ray diffraction (Fig. 1), well crystallized  $\text{MnCO}_3$  and MnO are prepared, respectively, after precipitation and calcination. The peak at  $\sim 2\theta = 26.6^\circ$  corresponding to carbon nanotubes (CNTs) is also indexed for the composites. It is appreciably broadened possibly due to the defects created by functionalization of MWNTs. In addition, no other impurity is detected for all the samples. Moreover, the FESEM image in Fig. 2(a) shows that  $\text{MnCO}_3$  has a homogeneous spherical morphology with diameters

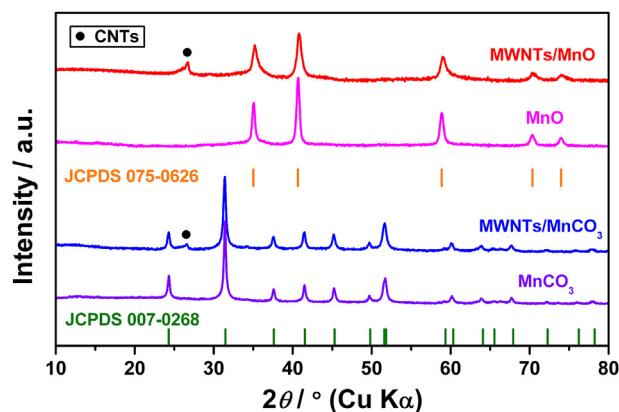


Fig. 1. XRD patterns of  $\text{MnCO}_3$ , MnO, MWNTs/ $\text{MnCO}_3$  and MWNTs/MnO. The vertical lines indicate the reference patterns of  $\text{MnCO}_3$  (JCPDS 007-0268) and MnO (JCPDS 075-0626).

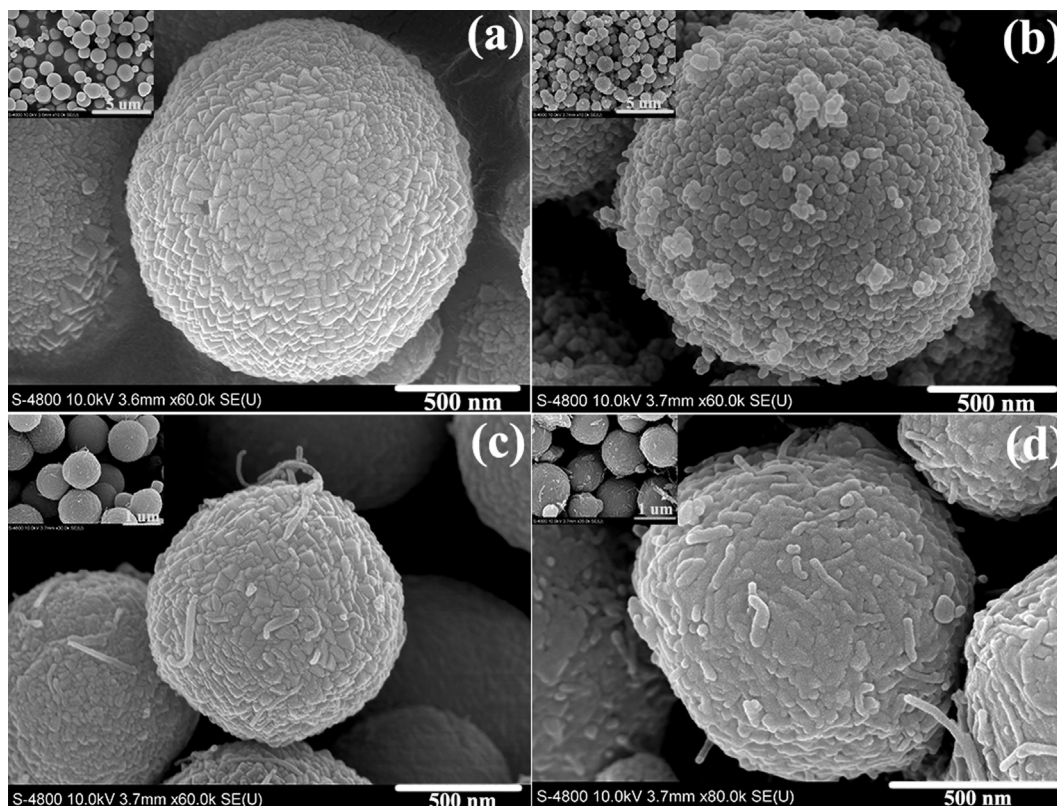


Fig. 2. FESEM images of  $\text{MnCO}_3$  (a),  $\text{MnO}$  (b), MWNTs/ $\text{MnCO}_3$  (c) and MWNTs/ $\text{MnO}$  (d). The insets display the morphologies at a lower magnification.

of about 1.4–1.5  $\mu\text{m}$ . The primary particles constructing the spheres are sized between 40 and 50 nm. Such unique particle shape is generally kept in subsequently obtained  $\text{MnO}$  (Fig. 2(b)). Compared with the  $\text{MnCO}_3$  precursor, the primary particles of  $\text{MnO}$  are loosely packed to form the secondary microspheres, which are very probably caused by  $\text{CO}_2$  releasing during calcination [11]. As can be seen from Fig. 2(c) and (d), the spherical morphology is not changed by combing with carbon nanotubes, and uniform MWNTs/ $\text{MnCO}_3$  spheres and MWNTs/ $\text{MnO}$  spheres are observed, respectively. But the secondary particle size is only  $\sim 1.0$ – $1.2 \mu\text{m}$  for both of them, which is slightly smaller than that of their counterparts without MWNTs. Carbon nanotubes therefore might affect the

crystal growth of  $\text{MnCO}_3$  in the composite during precipitation. Fig. 3 shows the EDX spectrogram on a selected area of MWNTs/ $\text{MnO}$ . The signal of deposited platinum (Pt) for easier FESEM measurement is also detected. Despite the inaccuracy of quantitative analysis of EDX technique, the large amounts of Mn and O on the surface of MWNTs indicate that CNTs are coated by manganese oxide. The MWNTs coated by  $\text{MnO}$  are then connected together to form the spherical MWNTs/ $\text{MnO}$  composite.

The lithium cyclability of manganese carbonate ( $\text{MnCO}_3$ ) is seldom investigated. Based on traditional conversion reaction yielding  $\text{LiCO}_3$  and Mn metal, the theoretical specific capacity of  $\text{MnCO}_3$  is  $466 \text{ mA h g}^{-1}$ . However, Tirado's group [33] practically

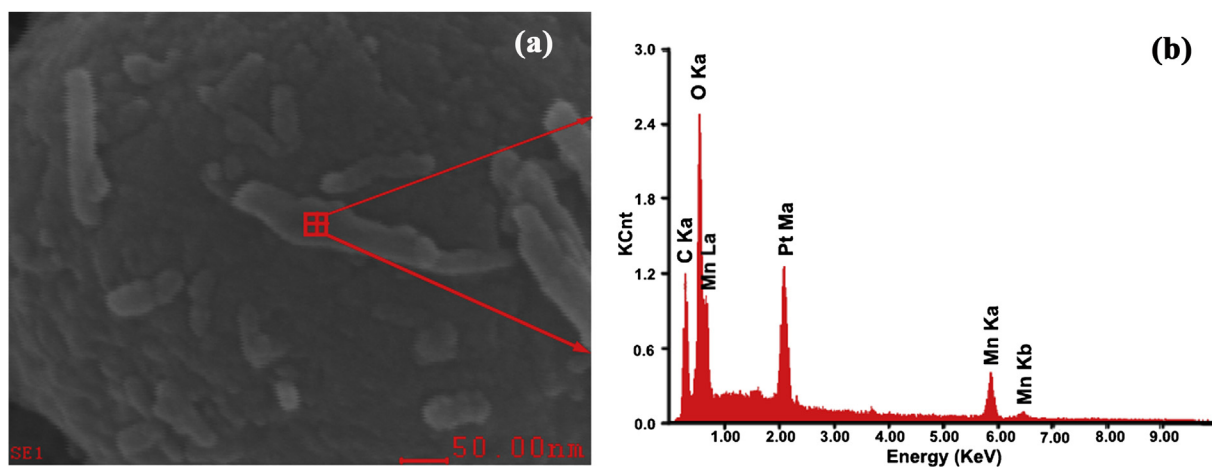


Fig. 3. EDX spectrum (b) of MWNTs/ $\text{MnO}$  on the selected area (a).



achieved a first charge capacity of  $\sim 600 \text{ mA h g}^{-1}$  at 0.25 C in the potential range of 0–3.0 V. To our knowledge, little electrochemical data is available since then. Here, we investigated the battery performance of  $\text{MnCO}_3$  between 0.01 V and 3.0 V (Fig. 4). In the first 5 cycles, the discharge/charge current density is  $30 \text{ mA g}^{-1}$ . The reversible specific capacity of the first cycle is  $\sim 635 \text{ mA h g}^{-1}$  which is in good agreement with Tirado's work [33]. Nonetheless, the initial coulombic efficiency (charge capacity divided by discharge capacity) is only  $\sim 39\%$ , and the capacity is dramatically decreased to  $\sim 424 \text{ mA h g}^{-1}$  after 5 cycles. At a higher current density of  $60 \text{ mA g}^{-1}$ , the specific capacity is dropped from  $\sim 323 \text{ mA h g}^{-1}$  to  $\sim 164 \text{ mA h g}^{-1}$  after 90 cycles corresponding to a capacity retention of only  $\sim 51\%$ . Take the first and sixth cycle in Fig. 4(a) as examples, coincidentally  $\sim 51\%$  of the capacity is lost when the current density is doubled. The large capacity degradation along with cycling and the inferior rate capability might be the reason of the tardy development of  $\text{MnCO}_3$  anode. Fig. 4(b) depicts the discharge/charge curves of  $\text{MnCO}_3$  at selected cycles. During first discharging, three distinct potential regions are notified. The first plateau at  $\sim 1.3\text{--}1.2 \text{ V}$  corresponds to the formation of SEI (solid electrolyte interface) layer [8] which contributes an irreversible capacity of about  $135 \text{ mA h g}^{-1}$ . The second plateau at  $\sim 0.4\text{--}0.3 \text{ V}$  corresponds to  $\text{Li}^+$  insertion into the host material by transformation of  $\text{MnCO}_3$  into  $\text{LiCO}_3$  and Mn, which provides most of the reversible capacity. The slope line thereafter from  $\sim 0.3 \text{ V}$  up to the cutoff (0.01 V) is the third region where  $\text{Li}^+$  is further incorporated by an interfacial storage mechanism [34]. During

charging, the average  $\text{Li}^+$  extraction potential is found to be about 1.43 V.

As can be seen from Fig. 5, the electrochemical performance of  $\text{MnCO}_3$  is much improved by compositing with MWNTs. At a current density of  $35 \text{ mA g}^{-1}$ , the reversible capacity between 0.01 V and 3.0 V could reach  $\sim 688 \text{ mA h g}^{-1}$  and  $\sim 440 \text{ mA h g}^{-1}$  in the first and fifth cycle, respectively. The initial coulombic efficiency is  $\sim 48\%$ . All these values are higher than that of bare  $\text{MnCO}_3$  in Fig. 4 although they are acquired at a higher current density (vs.  $30 \text{ mA g}^{-1}$  in Fig. 4). During the subsequent long-term cycling, the specific capacity is slightly increased from  $\sim 328 \text{ mA h g}^{-1}$  to  $\sim 351 \text{ mA h g}^{-1}$  in the initial 30 cycles, and is slowly decreased thereafter to  $\sim 298 \text{ mA h g}^{-1}$  at the end of 205 cycles. The capacity retention is  $\sim 91\%$  indicating a capacity loss of  $\sim 0.05\%$  per cycle. Note also that the current density is more than twice of that of  $\text{MnCO}_3$  for long-term cycling in Fig. 4. The discharge/charge curves (Fig. 5(b)) have similar trends with that of  $\text{MnCO}_3$  (Fig. 4(b)) except that the irreversible capacity caused by SEI formation is larger because of the contribution from MWNTs [35]. Therefore, both the cycling and rate performances of  $\text{MnCO}_3$  are evidently improved by MWNTs. Unfortunately, the initial efficiency of 48% is still too low for practical application.

Fig. 6 shows the battery performance of bare MnO decomposed from  $\text{MnCO}_3$ . In the first 5 cycles, the reversible specific capacity decreases from  $\sim 895 \text{ mA h g}^{-1}$  to  $\sim 747 \text{ mA h g}^{-1}$  at the current density of  $35 \text{ mA g}^{-1}$  with an initial coulombic efficiency of  $\sim 64\%$ . In the subsequent 90 cycles, it recedes from  $\sim 597 \text{ mA h g}^{-1}$  to  $\sim 237 \text{ mA h g}^{-1}$  with a capacity retention of  $\sim 40\%$  at the current

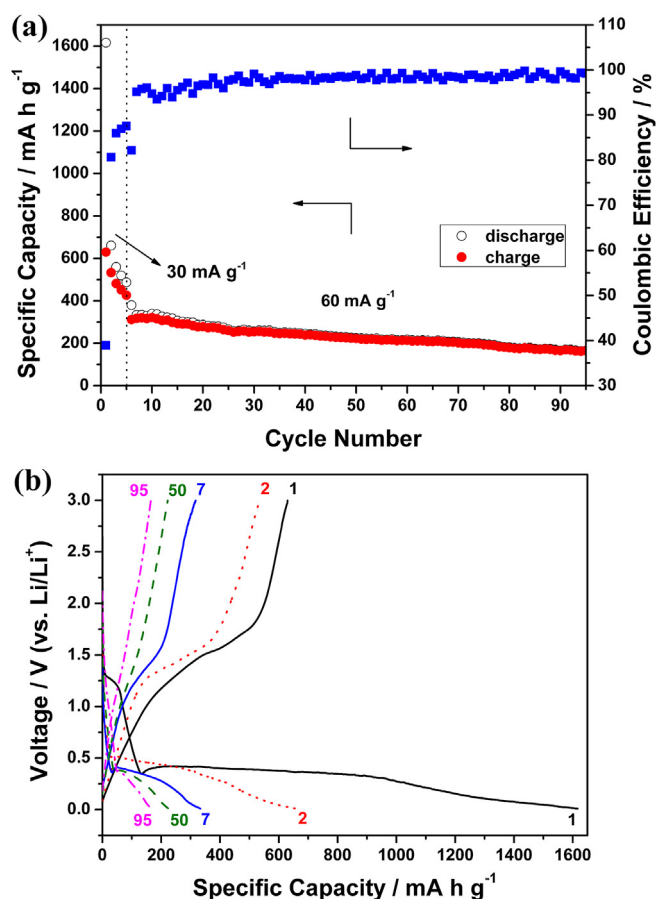


Fig. 4. The lithium cyclability of  $\text{MnCO}_3$  (a) with discharge/charge curves at selected cycles noted by numbers (b).

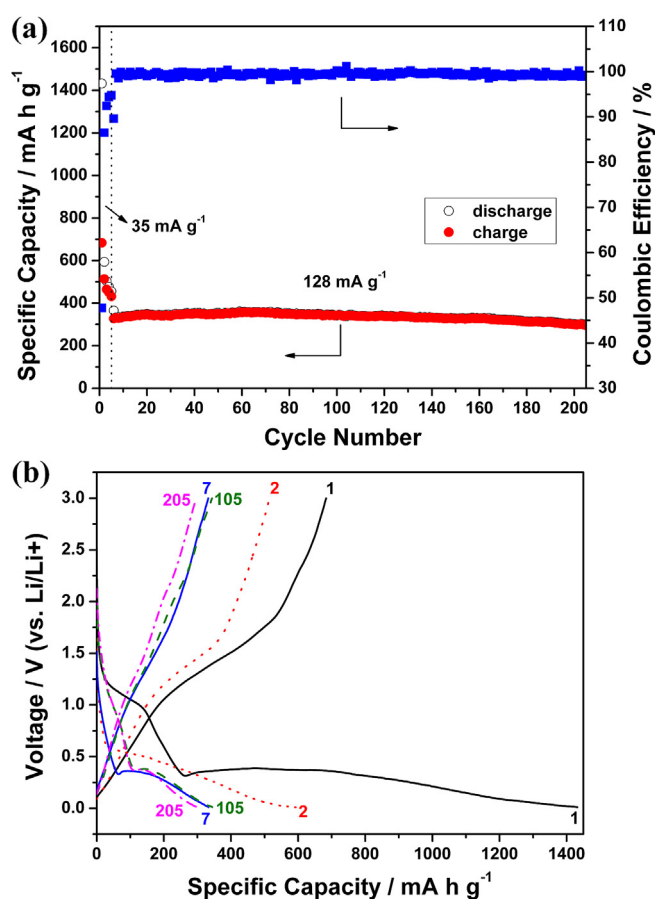


Fig. 5. The lithium cyclability of MWNTs/ $\text{MnCO}_3$  (a) with discharge/charge curves at selected cycles noted by numbers (b).

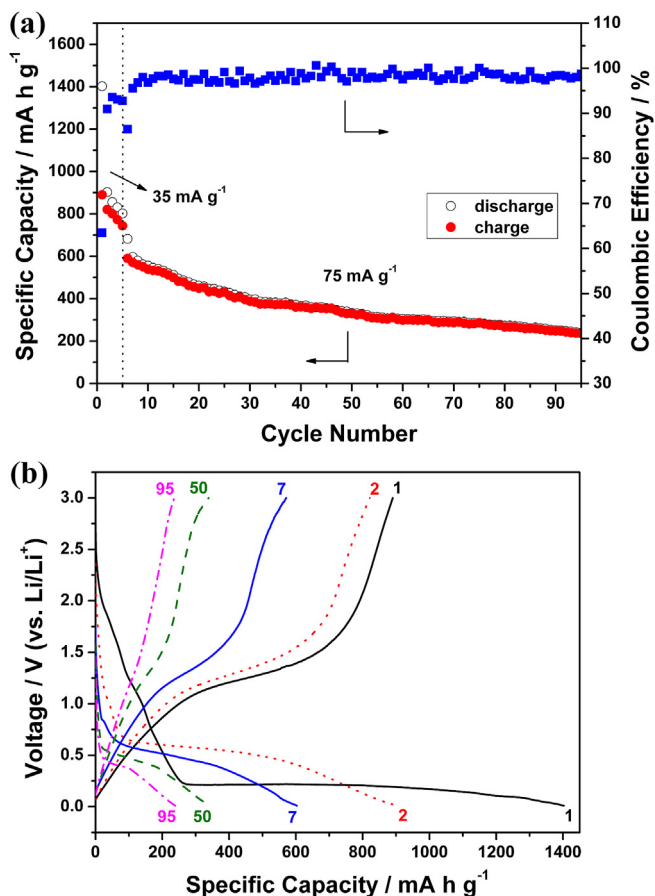


Fig. 6. The lithium cyclability of MnO (a) with discharge/charge curves at selected cycles noted by numbers (b).

density of  $75 \text{ mA g}^{-1}$ . In comparison with the previous  $\text{MnCO}_3$ , the specific capacity is much higher while the cycling stability needs to be ameliorated. More importantly, the initial efficiency is tremendously improved even comparing with  $\text{MWNTs/MnCO}_3$ . During first discharge (Fig. 6(b)), SEI formation and interfacial lithium storage are also involved in the major conversion reaction of  $\text{MnO}$  ( $\text{MnO} + 2\text{Li}^+ + 2\text{e}^- \rightarrow \text{Mn} + \text{Li}_2\text{O}$ ). Reversed reaction takes place during charging by oxidation of  $\text{Mn}$  ( $\text{Mn} + \text{Li}_2\text{O} \rightarrow \text{MnO} + 2\text{Li}^+ + 2\text{e}^-$ ). The initial discharge potential plateau is  $\sim 0.23 \text{ V}$ , and is raised up to  $\sim 0.50 \text{ V}$  from the second cycle. The nano-miniatured  $\text{Mn}$  metal and  $\text{Li}_2\text{O}$  after first discharge are ascribed for such potential shift commonly existed in transition metal oxide anodes [36]. The average charge plateau of  $\text{MnO}$  is  $\sim 1.25 \text{ V}$ , which is lower not only than that of the previous  $\text{MnCO}_3$ , but also than that of a lot of well-known transition metal oxides such as  $\text{RuO}_2$  [37],  $\text{Co}_3\text{O}_4$  [38] and  $\text{CuO}$  [39]. The discharge voltages of full batteries paired with  $\text{MnO}$  anodes are therefore fairly elevated, so do the energy densities. In addition to low cost and environmental benignity,  $\text{MnO}$  is thus expected as an attractive candidate anode material for future lithium-ion batteries among various transition metal oxides.

In analogy of  $\text{MWNTs/MnCO}_3$  composite, the electrochemical performance of  $\text{MnO}$  sphere is also remarkably improved by supporting with  $\text{MWNTs}$  conducting networks. As shown in Fig. 7(a), the reversible specific capacity of the first, second and fifth cycle is  $\sim 1005 \text{ mA h g}^{-1}$ ,  $\sim 1036 \text{ mA h g}^{-1}$  and  $\sim 989 \text{ mA h g}^{-1}$ , respectively, when discharged/charged constantly at  $35 \text{ mA g}^{-1}$ . The imperceptible capacity increase from the first cycle to the second cycle is attributed to synergetic lithium storage of each component

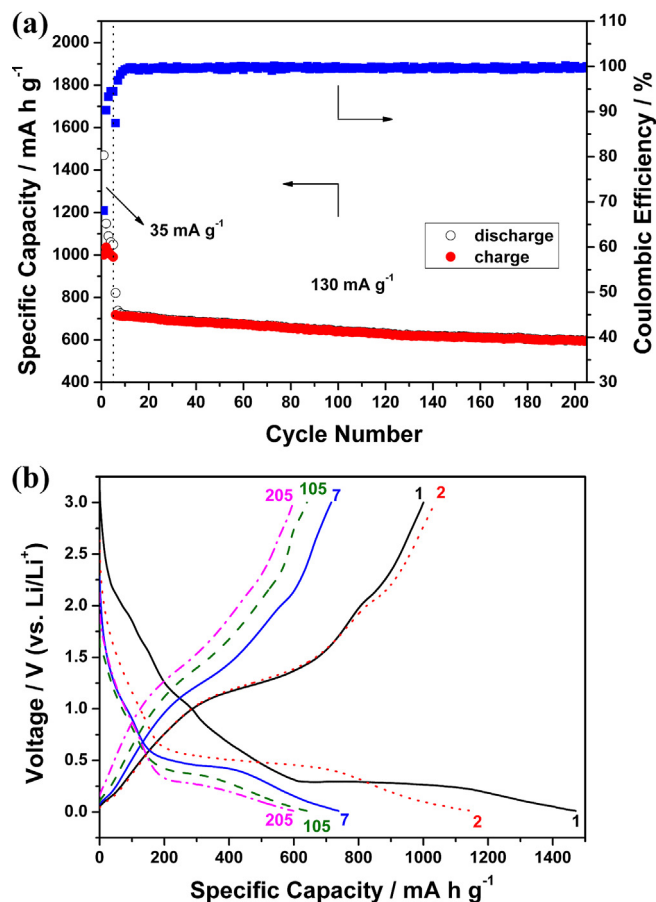


Fig. 7. The lithium cyclability of  $\text{MWNTs/MnO}$  (a) with discharge/charge curves at selected cycles noted by numbers (b).

in the electrode [30]. The initial coulombic efficiency is  $\sim 69\%$ . At a higher current density of  $130 \text{ mA g}^{-1}$ , the specific capacity is slowly degraded from  $\sim 722 \text{ mA h g}^{-1}$  to  $\sim 597 \text{ mA h g}^{-1}$  after 200 cycles. The capacity retention is  $\sim 83\%$  indicating that about  $\sim 0.09\%$  capacity is lost per cycle. The discharge/charge curves (Fig. 7(b)) are similar to that of  $\text{MnO}$  (Fig. 6(b)). The potential hysteresis calculated from the discharge/charge curves of the second cycle is about  $0.7 \text{ V}$ . Therefore,  $\text{MWNTs/MnO}$  exhibits the best battery performance among the 4 materials studied in this paper. However, the initial coulombic efficiency still needs to be improved and the potential hysteresis needs to be significantly reduced for practical applications.

The same prototype battery was further galvanostatically discharged/charged at different current densities to fully investigate the rate capability of  $\text{MWNTs/MnO}$ . The results are shown in Fig. 8. The typical charge capacity at  $45 \text{ mA g}^{-1}$ ,  $80 \text{ mA g}^{-1}$ ,  $145 \text{ mA g}^{-1}$ ,  $315 \text{ mA g}^{-1}$ ,  $540 \text{ mA g}^{-1}$  and  $715 \text{ mA g}^{-1}$  is  $\sim 904 \text{ mA h g}^{-1}$ ,  $\sim 831 \text{ mA h g}^{-1}$ ,  $\sim 708 \text{ mA h g}^{-1}$ ,  $\sim 577 \text{ mA h g}^{-1}$ ,  $\sim 474 \text{ mA h g}^{-1}$  and  $\sim 447 \text{ mA h g}^{-1}$ , respectively. From  $45 \text{ mA g}^{-1}$  to  $715 \text{ mA g}^{-1}$ , nearly 15 times of the current is increased, but more than half of the capacity could still be obtained.  $1\text{C}$  rate is usually used in industry to evaluate the rate performance of lithium-ion batteries. Here,  $\text{MWNTs/MnO}$  delivers a reversible capacity of  $\sim 447 \text{ mA h g}^{-1}$  at  $\sim 1.6 \text{ C}$  rate ( $715 \text{ mA g}^{-1}$ ), which is even larger than the theoretical number of commercial graphite ( $372 \text{ mA h g}^{-1}$ ). When the current density is turned back to  $45 \text{ mA g}^{-1}$ , a specific charge capacity of  $\sim 802 \text{ mA h g}^{-1}$  is recovered. In addition to suffering all the rigid measurements in Figs. 7 and 8, the lost capacity is also probably

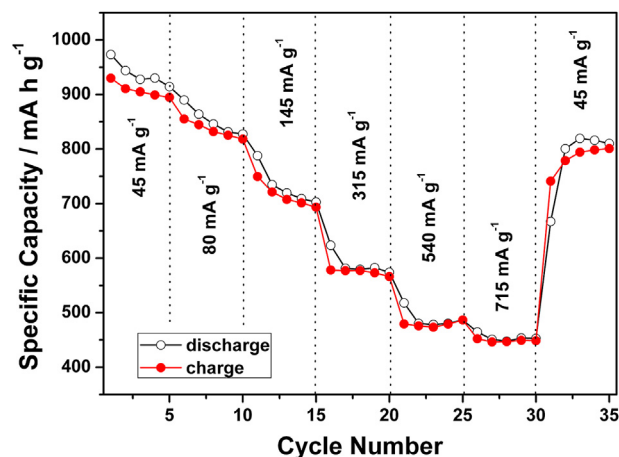


Fig. 8. Rate capability of MWNTs/MnO. The potential window is 0.01–3.0 V (vs. Li/Li<sup>+</sup>).

related to the conversion reaction nature of metal oxides during lithium insertion/extraction [40]. The cell was ultimately cycled at a high current density of 380 mA g<sup>-1</sup> in Fig. 9. The specific capacity is in reasonable agreement with Fig. 8 in consideration of rate capability. It slowly decreases from ~419 mA h g<sup>-1</sup> to ~373 mA h g<sup>-1</sup> after 100 cycles. The capacity retention is ~89%. Therefore, ~0.11% capacity is lost per cycle. The robust battery performance is a great advancement to that of our previous MWNTs/MnO composite rods [29].

Electrochemical impedance spectroscopy (EIS) [41] was carried out to understand the performance enhancement of MnO sphere by supporting with MWNTs backbones. The Nyquist plots of bare MnO and MWNTs/MnO are shown in Fig. 10. The spectra were collected at the charged state before/after 5 cycles. All the profiles generally have a depressed semicircle in the high frequency region and a slope line in the low frequency region. The former is associated with charge transfer resistance ( $R_{ct}$ ), and the latter is attributed to lithium diffusion into the bulk materials (Warburg impedance) [42]. The  $R_{ct}$  of MnO is reduced from ~526  $\Omega$  to ~82  $\Omega$  after 5 cycles while that of MWNTs/MnO is reduced from ~297  $\Omega$  to ~35  $\Omega$ . The charge transfer resistance is reduced in several cycles along with cycling due to the activation of electrode materials [30]. As has been widely demonstrate in literature [43–45], the inherent high conductivity of carbon nanotubes facilitates efficient electron transfer and transportation in the composite spheres by direct

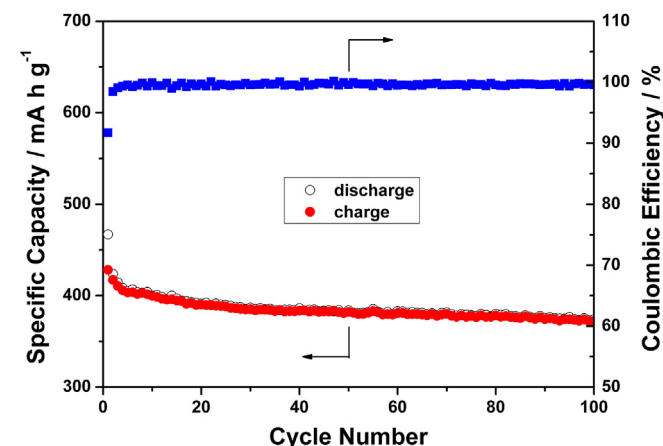


Fig. 9. Cycling performance of MWNTs/MnO at a higher current density of 380 mA g<sup>-1</sup>. The potential window is 0.01–3.0 V (vs. Li/Li<sup>+</sup>).

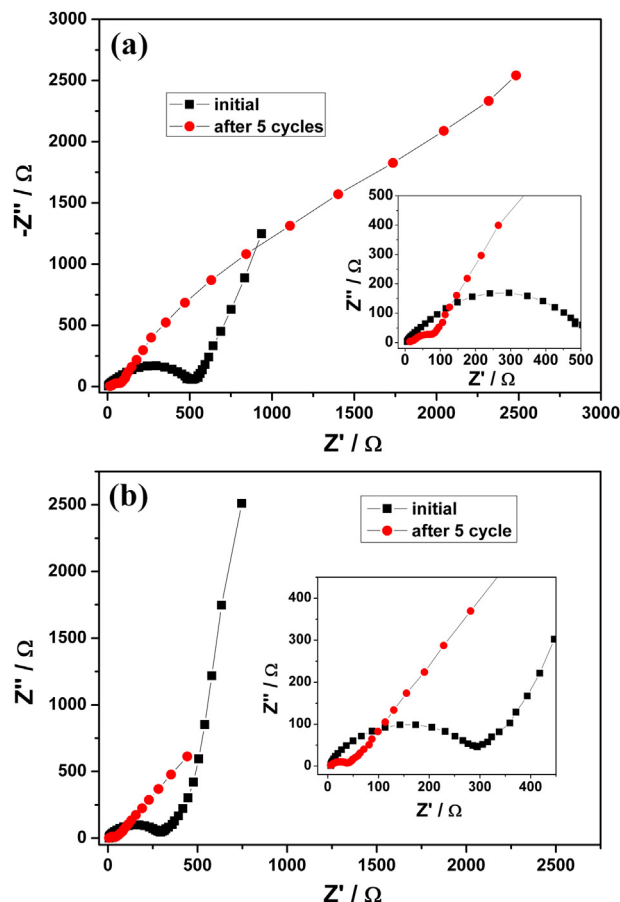


Fig. 10. EIS spectra of MnO (a) and MWNTs/MnO (b) before and after 5 cycles. Data were collected between 10<sup>5</sup> Hz and 10<sup>-2</sup> Hz at the charged state after a stabilization of 2 h.

interconnections between MWNTs and metal oxides. As a result, the  $R_{ct}$  of MWNTs/MnO both at fresh OCP (open circuit potential) and after 5 cycles is significantly reduced comparing with that of bare MnO. The intimate interaction of MWNTs with nano-MnO could accommodate the large volume change of MnO during Li<sup>+</sup> incorporation and extraction [46], and contribute extra capacities based on synergetic lithium storage [30,34] via conversion, interfacial and insertion reactions. The conversion and interfacial reactions are contributed by MnO as identified earlier in Fig. 4 (b) while the insertion reaction mainly comes from CNTs [44]. Meanwhile, MWNTs supported microsphere MnO has a tap density of about 1.6 g cm<sup>-3</sup>, therefore, is expected to hold a large volumetric energy density [47,48] comparing with graphite. Such unique advantages make MWNTs/MnO composite sphere an attractive candidate anode material for next generation lithium-ion batteries.

#### 4. Conclusions

The electrochemical performance of both MnCO<sub>3</sub> and MnO could be significantly improved by forming composite spheres with MWNTs. The embedded carbon nanotubes could enable efficient charge transfer in the electrode/electrolyte interface, buffer the large volume expansion/contraction during Li<sup>+</sup> insertion/extraction, and offer extra capacities by synergetic lithium storage. Comparing with MWNTs/MnCO<sub>3</sub>, MWNTs/MnO composite sphere shows a lower charging potential, a higher reversible capacity and a faster rate capability with good cycling stability. Future efforts need

to be put on further improving the initial coulombic efficiency while minimizing the potential hysteresis for practical application of the MWNTs/MnO anode.

## Acknowledgements

The authors would thank Ms. Lijing Ma from the State Key Laboratory of Multiphase Flow in Power Engineering at Xi'an Jiaotong University for technical help on X-ray diffraction. Ms. Yanling Liu at The Fourth Military Medical University is appreciated for her help on FESEM and EDX measurements.

## References

- [1] J.B. Goodenough, Y. Kim, *Chem. Mater.* 22 (2010) 587–603.
- [2] M. Armand, J.M. Tarascon, *Nature* 451 (2008) 652–657.
- [3] Y.P. Wu, E. Rahm, R. Holze, *J. Power Sources* 114 (2003) 228–236.
- [4] K. Ariyoshi, R. Yamato, T. Ohzuku, *Electrochim. Acta* 51 (2005) 1125–1129.
- [5] K. Kravchuk, L. Protesescu, M.I. Bodnarchuk, F. Krumeich, M. Yarema, M. Walter, C. Guntlin, M.V. Kovalenko, *J. Am. Chem. Soc.* 135 (2013) 4199–4202.
- [6] H. Wu, G. Yu, L. Pan, N. Liu, M.T. McDowell, Z. Bao, Y. Cui, *Nat. Commun.* 4 (2013).
- [7] M.V. Reddy, G.V. Subba Rao, B.V.R. Chowdari, *Chem. Rev.* 113 (2013) 5364–5457.
- [8] P. Poizot, S. Laruelle, S. Grugeon, L. Dupont, J.M. Tarascon, *Nature* 407 (2000) 496–499.
- [9] J. Cabana, L. Monconduit, D. Larcher, M.R. Palacin, *Adv. Mater.* 22 (2010) E170–E192.
- [10] K. Zhong, X. Xia, B. Zhang, H. Li, Z. Wang, L. Chen, *J. Power Sources* 195 (2010) 3300–3308.
- [11] K. Zhong, B. Zhang, S. Luo, W. Wen, H. Li, X. Huang, L. Chen, *J. Power Sources* 196 (2011) 6802–6808.
- [12] B. Sun, Z. Chen, H.-S. Kim, H. Ahn, G. Wang, *J. Power Sources* 196 (2011) 3346–3349.
- [13] X. Fang, X. Lu, X. Guo, Y. Mao, Y.-S. Hu, J. Wang, Z. Wang, F. Wu, H. Liu, L. Chen, *Electrochim. Commun.* 12 (2010) 1520–1523.
- [14] C. Changju, P. Hongyeol, K. Dongwook, K. Jongsik, O. Eun-Suok, L. Jung Kyoo, *J. Power Sources* 244 (2013) 214–221.
- [15] P. Ding, Y.L. Xu, X.F. Sun, *Acta Phys. Chim. Sin.* 29 (2013) 293–297.
- [16] Y. Liu, X. Zhao, F. Li, D. Xia, *Electrochim. Acta* 56 (2011) 6448–6452.
- [17] J. Jiang, Y. Li, J. Liu, X. Huang, C. Yuan, X.W. Lou, *Adv. Mater.* 24 (2012) 5166–5180.
- [18] L.W. Ji, Z. Lin, M. Alcoutlabi, X.W. Zhang, *Energy Environ. Sci.* 4 (2011) 2682–2699.
- [19] X. Zhang, Z. Xing, L. Wang, Y. Zhu, Q. Li, J. Liang, Y. Yu, T. Huang, K. Tang, Y. Qian, X. Shen, *J. Mater. Chem.* 22 (2012) 17864–17869.
- [20] G.-L. Xu, Y.-F. Xu, H. Sun, F. Fu, X.-M. Zheng, L. Huang, J.-T. Li, S.-H. Yang, S.-G. Sun, *Chem. Commun.* 48 (2012) 8502–8504.
- [21] Y.L. Ding, C.Y. Wu, H.M. Yu, J. Xie, G.S. Cao, T.J. Zhu, X.B. Zhao, Y.W. Zeng, *Electrochim. Acta* 56 (2011) 5844–5848.
- [22] X. Li, D. Li, L. Qiao, X. Wang, X. Sun, P. Wang, D. He, *J. Mater. Chem.* 22 (2012) 9189–9194.
- [23] Y.J. Mai, D. Zhang, Y.Q. Qiao, C.D. Gu, X.L. Wang, J.P. Tu, *J. Power Sources* 216 (2012) 201–207.
- [24] C.-T. Hsieh, C.-Y. Lin, J.-Y. Lin, *Electrochim. Acta* 56 (2011) 8861–8867.
- [25] G. Yang, Y. Li, H. Ji, H. Wang, P. Gao, L. Wang, H. Liu, J. Pinto, X. Jiang, *J. Power Sources* 216 (2012) 353–362.
- [26] Y. Xia, Z. Xiao, X. Dou, H. Huang, X.H. Lu, R.J. Yan, Y.P. Gan, W.J. Zhu, J.P. Tu, W.K. Zhang, X.Y. Tao, *ACS Nano* 7 (2013) 7083–7092.
- [27] X.Q. Yu, Y. He, J.P. Sun, K. Tang, H. Li, L.Q. Chen, X.J. Huang, *Electrochim. Commun.* 11 (2009) 791–794.
- [28] Z.H. Cui, X.X. Guo, H. Li, *J. Power Sources* 244 (2013) 731–735.
- [29] X. Sun, Y. Xu, P. Ding, M. Jia, G. Ceder, *J. Power Sources* 244 (2013) 690–694.
- [30] X. Sun, Y. Xu, P. Ding, G. Chen, X. Zheng, *Mater. Lett.* 113 (2013) 186–189.
- [31] X.F. Sun, Y.L. Xu, J. Wang, *J. Solid State Electrochem.* 16 (2012) 1781–1789.
- [32] X.F. Sun, Y.L. Xu, J. Wang, S.C. Mao, *Int. J. Electrochem. Sci.* 7 (2012) 3205–3214.
- [33] M.J. Aragon, C. Perez-Vicente, J.L. Tirado, *Electrochim. Commun.* 9 (2007) 1744–1748.
- [34] J.-Y. Shin, D. Samuelis, J. Maier, *Adv. Funct. Mater.* 21 (2011) 3464–3472.
- [35] C. Kang, I. Lahiri, R. Baskaran, W.-G. Kim, Y.-K. Sun, W. Choi, *J. Power Sources* 219 (2012) 364–370.
- [36] C. Ban, Z. Wu, D.T. Gillaspie, L. Chen, Y. Yan, J.L. Blackburn, A.C. Dillon, *Adv. Mater.* 22 (2010) E145.
- [37] P. Balaya, H. Li, L. Kienle, J. Maier, *Adv. Funct. Mater.* 13 (2003) 621–625.
- [38] N. Yan, L. Hu, Y. Li, Y. Wang, H. Zhong, X. Hu, X. Kong, Q. Chen, *J. Phys. Chem. C* 116 (2012) 7227–7235.
- [39] C. Xin, Z. Naigang, S. Kening, *J. Mater. Chem.* 22 (2012) 15080–15084.
- [40] X.F. Li, C.L. Wang, *J. Mater. Chem. A* 1 (2013) 165–182.
- [41] X. Sun, Y. Xu, M. Jia, P. Ding, Y. Liu, K. Chen, *J. Mater. Chem. A* 1 (2013) 2501–2507.
- [42] Y. Liu, Y. Xu, X. Sun, *Funct. Mater. Lett.* 6 (2013) 1350053.
- [43] X.F. Li, A. Dhanabalan, L. Gu, C.L. Wang, *Adv. Energy Mater.* 2 (2012) 238–244.
- [44] X.F. Li, J. Liu, Y. Zhang, Y.L. Li, H. Liu, X.B. Meng, J.L. Yang, D.S. Geng, D.N. Wang, R.Y. Li, X.L. Sun, *J. Power Sources* 197 (2012) 238–245.
- [45] X.M. Liu, Z.D. Huang, S.W. Oh, B. Zhang, P.C. Ma, M.M.F. Yuen, J.K. Kim, *Compos. Sci. Technol.* 72 (2012) 121–144.
- [46] P. Zhang, Y. Wang, X. Ren, K. Liu, S. Chen, *J. Power Sources* 233 (2013) 166–173.
- [47] Y.-K. Sun, S.-M. Oh, H.-K. Park, B. Scrosati, *Adv. Mater.* 23 (2011) 5050–5054.
- [48] X.F. Sun, Y.L. Xu, Y.H. Liu, L. Li, *Acta Phys. Chim. Sin.* 28 (2012) 2885–2892.